# UC Irvine

**Title**
Orientation-Dependent Handedness of Chiral Plasmons on Nanosphere Dimers: How to Turn a Right Hand into a Left Hand

**Authors**
Banik, Mayukh
Rodriguez, Kate
Hulkko, Eero
et al.

# Orientation-Dependent Handedness of Chiral Plasmons on Nanosphere Dimers: How to Turn a Right Hand into a Left Hand

Mayukh Banik,[†] Kate Rodriguez,[†] Eero Hulkko,[†,‡] and V. Ara Apkarian*,[†]

[†]Department of Chemistry, University of California, Irvine, California 92697-2025, United States
[‡]Nanoscience Center, Department of Physics, University of Jyvaskyla, P.O. Box 35, Jyvaskyla FI-40014, Finland

**S** *Supporting Information*

**ABSTRACT:** Optical activity, which is used as a discriminator of chiral enantiomers, is demonstrated to be orientation dependent on individual, and nominally achiral, plasmonic nanosphere dimers. Through measurements of their giant Raman optical activity, we demonstrate that L/R-handed enantiomers can be continuously turned into their R/L-handed mirror images without passing through an achiral state. The primitive uniaxial multipolar response, with demonstrable broken parity and time reversal symmetry, reproduces the observations as resonant Raman scattering on plasmons that carry angular momentum. The analysis underscores that chirality does not have a quantitative continuous measure and recognizes the manipulation of superpositions of multipolar plasmons as a paradigm for novel optical materials with artificial magnetism.

**KEYWORDS:** *chiral connectedness, Raman optical activity, multipolar Raman, nonreciprocal, PT invariance, chiroptical activity*
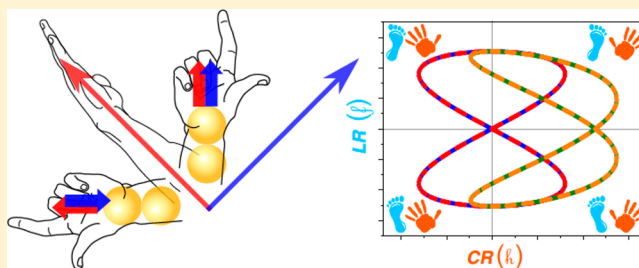
We primarily see through the electric component of electromagnetic waves, and this is formally stated by setting the magnetic permeability of homogeneous continuous media to unity at optical frequencies.[1] The consideration changes on metallic nanostructures, which individually act as nanoantennas (nantennas)[2] and collectively, serve as meta-materials with optical properties that can be tuned by their architecture.[3] Nanostructuring alone opens up the magnetic channel of light−matter interaction.[4,5] This is impressed by the illustration in Figure 1, where in the limit $2\pi r/\lambda \approx 1$, the E-field
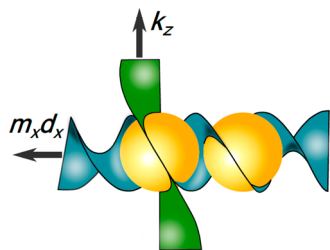


**Figure 1.** Chiral induction due to spatial dispersion. The electric field of circularly polarized light (green ribbon) propagating along the z-axis traces a helical trajectory on the surface of a nanosphere. The induced helical surface current is extended (blue ribbon) beyond the nanospheres for clarity. It represents a chiral plasmon, which carries collinear magnetic and electric fields normal to incidence and handedness given by the pseudoscalar $h = \hat{m} \cdot \hat{d}$, the product of induced magnetic and electric dipoles. The assumed scaling factor for the light−matter interaction is $\zeta = kr = 2\pi r/\lambda \approx 0.6$, consistent with the experimental system and representative of optical nantennas, e.g., a nanosphere of radius $r = 50$ nm and light of $\lambda = 500$ nm.

of circularly polarized light is seen to trace a helix on the surface of a nanosphere. The induced helical surface current is a chiral plasmon that carries collinear E and B fields due to the coupled linear and angular displacement: Due to length scales alone, the electric component of light generates large magnetic fields at optical frequencies in an otherwise nonmagnetic material. Such artificial magnetism is key to the design of optically active metamaterials,[6,7] as in negative index media[8] that allow left-handed propagation of light[9,10] and cloaking,[11] nonreciprocal response that breaks time reversal symmetry,[12−14] and chiroptical response that provides a general route to optical activity and control over polarization states of light.[15,16] The obvious strategy toward the design of chiroptical media is to rely on chiral architectures that lack reflection symmetry, and a wide range of systems have been realized in this category,[7,17] be it single nantennas,[18−21] planar arrays,[22,23] or 3D structures.[24] More intriguing is the optical activity of achiral structures, where the requisite broken symmetries derive from the light−matter interaction.[20,25] Here, we show that nominally achiral nanosphere dimers (nanodumbbell), consisting of $r = 50$ nm gold spheres separated by a 1 nm gap,[26] exhibit giant, orientation-dependent, nonreciprocal, chiroptical response. The activity can be attributed to chiral plasmons, prepared by the superposition of collinear electric and magnetic dipole excitation. This could have been anticipated by recognizing that the nanodumbbell is at once the miniature of the Hertzian dipole antenna[27] and the macroanalogue of diatomic

molecules[28] that sustain angular momentum states quantized along their internuclear axis.

Through polarization-dependent inelastic light scattering measurements (see Methods) we establish that nominally achiral nanodumbbells show giant Raman optical activity (ROA),[29] with orientation-dependent handedness (ODH) in their response. This is illustrated in Figure 2, where we show
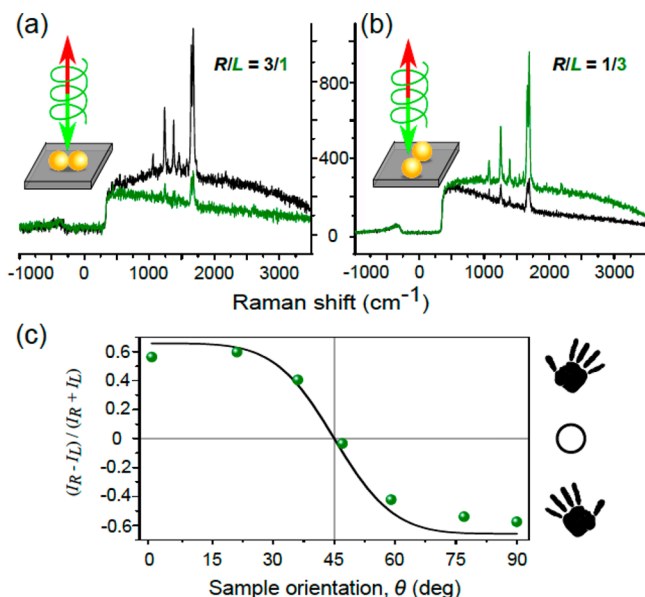


**Figure 2.** Orientation-dependent handedness. Backscattered Raman spectra recorded with circularly polarized incident light, RCP (black trace) and LCP (green trace), are shown on a nanodumbbell oriented at $\theta = 0°$ in (a) and at $\theta = 90°$ in (b). The sharp lines belong to the vibrational SERS of the achiral molecular load, *trans*-bipyridylethylene, which rides over the electronic Raman scattering continuum of the nantenna. (a) At $\theta = 0$, the response is R-handed, as judged by the intensity ratio R/L = 3/1; (b) at $\theta = 90°$, the response inverts to L-handed, with intensity ratio R/L = 1/3. (c) Continuous evolution of the handedness in circular ROA, CR = $(I_R − I_L)/(I_R + I_L)$ as a function of the rotation angle $\theta$ of the nanodumbbell in the plane perpendicular to incidence. The response is R-handed for CR > 0, L-handed for CR < 0, and not handed at CR = 0, at $\theta = 45°$. The measured experimental points (green circles) are overlaid on the analytic function of the scattering matrix extracted from the two-parameter fit to the data set (see text).

backscattered Raman spectra recorded with circularly polarized light (Figure 2a,b). They consist of the plasmon-enhanced vibrational Raman spectrum (SERS) of the achiral molecular load, *trans*-bipyridylethylene,[30] and the electronic Raman scattering (ERS) continuum of the nantenna.[31] The ERS further decomposes into an isotropic and a chiral component, identifying two distinct plasmons.[32] The molecular spectrum tracks the response of the chiral plasmon. The spectra (all molecular lines) show a contrast ratio of 3:1 when excited with L/R-polarization, which is a giant effect when compared to typical ROA values of $10^{-3}–10^{-5}$ in molecular spectra.[29] Remarkably, the intensity ratio L:R = 3:1 inverts to L:R = 1:3 upon 90° rotation of the nanodumbbell in the plane normal to incidence, and, as seen in Figure 2c, L/R-handed dumbbells continuously turn R/L-handed upon their in-plane rotation. This would not be possible if optical activity was strictly structural in origin, which is a presumption ingrained by the traditional labeling of molecular enantiomers according to their

optical rotatory activity. Indeed, homochirality of life is contingent on chiral discrimination, which uniquely couples handedness in structure to response.[33] Given the impossibility of turning an R-handed screw L-handed by any whole body rotation, if chiral response of a solid body were determined by its structure, ODH would not be possible. Nevertheless, this is exactly what is observed in Figure 2.

The apparent paradox of ODH finds resolution on several levels. It touches on profound aspects of the universal asymmetry of chirality, which is ultimately traced to the parity violation of electroweak forces.[34] It also challenges notions based on Lord Kelvin's definition of chirality as broken mirror symmetry,[35] due to its reliance on the discrete symmetry operation of reflection in a perfect mirror as its measure. This was underscored in the recent demonstration of ODH by Efrati and Irvine, who introduced a quantitative continuous measure of handedness.[36] Ironically, although chirality is the generator of handedness, its quantification through a continuous measure remains illusive.[37] The challenge is closely associated with the paradox of chiral connectedness, whereby enantiomers may be interconverted without ever passing through an achiral state.[38] Indeed, the zero crossing seen in Figure 2c indicates that the response to circular polarization is not handed, but as we will see, not likely to be achiral. With these stipulations in mind, the contradictions of ODH are most gainfully resolved by noting that chirality in structure is determined by symmetries of the material Hamiltonian, while the response to a particular measurement is determined by the interaction Hamiltonian. The ground-state density of a nanodumbbell that describes its appearance (through elastic electron or photon scattering in a microscope) is a scalar function in Euclidian space. In contrast, interaction Hamiltonians are generally vectorial, and symmetry operations of rotation and reflection in Euclidian space need not have the same effect in vector space. We clarify these considerations through an explicit formulation of what may be regarded as the primitive chiroptical element of dispersive permeability, namely, the uniaxial electric dipole, magnetic dipole, and electric quadrupole $(d, m, q)$ response due to nonlocality (retardation) in the light−matter interaction. The helical induction of Figure 1 now arises from the quantum interference between magnetic and electric dipolar resonances. The model reproduces the inelastic light scattering data as resonant Raman scattering on plasmons that carry angular momentum, explains ODH, explicitly illustrates chiral connectedness, and recognizes the nanodumbbell as a flexible building block of optical metamaterials.

## ■ THE UNIAXIAL MULTIPOLE

Expansion of the electromagnetic vector potential to first order in spatial dispersion, $A = A_0 \hat{\varepsilon} \exp(\mathrm{i}k·r) \approx A_0 \hat{\varepsilon}(1 + \mathrm{i}k·r)$, leads to the well-known result for the light−matter interaction $A·\nabla$, as the sum[39]

$$\tilde{V} = \hat{\varepsilon}·\hat{d} + \frac{1}{2}\mathrm{i}\zeta(\hat{k} \times \hat{\varepsilon}·\hat{m} + \hat{\varepsilon}·\hat{q}·\hat{k}) \tag{1}$$

of electric dipole, E1, magnetic dipole, M1, and electric quadrupole, E2, transitions, respectively. The unitless potential, consists of a polar vector, axial vector, and a dyadic, with relative magnitudes $\zeta = kr = \langle m \rangle/\langle d \rangle = \langle q \rangle/\langle d \rangle$ that strictly hold when all three transitions are on resonance. Focusing on the experimental geometry of collinear scattering and incident light propagating along $\hat{z} = \hat{k}$ with transverse electric and magnetic fields given by the spinors
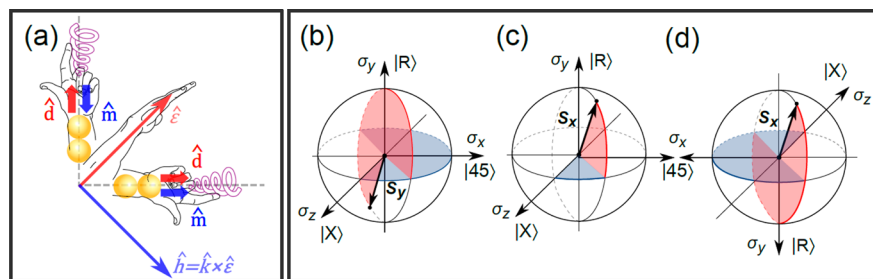
**Figure 3.** Euclidian versus spin-space representations of the interaction. (a) The helical current of linear ($d$ or $q$) and angular displacement ($m$) is generated by the projections of $\hat{\varepsilon}$ and $\hat{h}$ along the intersphere axis. Linearly polarized light along $\vartheta = 45°$ generates R/L-handed helicity, $\hat{m}\hat{d} = \pm 1$, on a dumbbell oriented along the $x/y$-axis. When aligned with the $E$-field, $\hat{h}\cdot\hat{n} = 0$, and $h = md/|m||d|$ is not defined. The vector-space (b, c, d) spanned by the Pauli spin matrices coincides with the orthogonal basis of the Stokes vector of light, as indicated by double labeling the axes. Measurements on nanodumbbells oriented along the laboratory $x,y$-axis correspond to projections of the incident Stokes vector on the antipodal pure states represented by the spin vectors $s_{x,y}$. They can be interconverted by inversion through the origin (b) ↔ (c) or by inversion of the frame, $\sigma_x, \sigma_y, \sigma_z \rightarrow -\sigma_x, -\sigma_y, -\sigma_z$ (d). Alternatively, $s_x$ can be converted into $s_y$ through the time reversal operator, $T = UK$, consisting of rotation $U$ in the real plane (gray) and reflection of the complex axis $\sigma_y \rightarrow -\sigma_y$. The continuous rotation of the nanodumbbell in the laboratory corresponds to travel on the chord that joins the antipodes, and measurements at angles $0 < \vartheta < \pi/2$ correspond to projections on mixed states (eq 3b). The chord passes through the origin, which corresponds to the achiral singularity, equivalent to projection on the racemic state at $\vartheta = \pi/4$.

$$\hat{\varepsilon} = \begin{bmatrix} e_x \\ e_y \end{bmatrix} \hat{k} \times \hat{\varepsilon} = \hat{h} = \begin{bmatrix} h_x \\ h_y \end{bmatrix} = \begin{bmatrix} -e_y \\ e_x \end{bmatrix} \tag{2}$$

the excitable moments are $d_i$, $m_i$, $q_{iz}$, with $i = x, y$, and the dyadic may be treated as polar vectors, $q_i \equiv q_{iz}$. Under the idealization that $d$, $m$, and $q$ lie along the intersphere axis, the observable excitation probabilities $\langle \Sigma_i \rangle \equiv \langle V_i^\dagger V_i \rangle$ can be cast in the form of 2D Jones matrices as a function of the orientation angle $\vartheta$ of the dimer in the laboratory:

$$\Sigma_\vartheta = \Sigma_X \cos^2 \vartheta + \Sigma_Y \sin^2 \vartheta \tag{3a}$$

where

$$\Sigma_X = \frac{1}{N}\begin{bmatrix} d^2 + q^2 & mq + imd \\ mq - imd & m^2 \end{bmatrix} \text{ and}$$

$$\Sigma_Y = \frac{1}{N}\begin{bmatrix} m^2 & -mq - imd \\ -mq + imd & d^2 + q^2 \end{bmatrix} \tag{3b}$$

are normalized ($N = d^2 + m^2 + q^2$), idempotent ($\Sigma_X^n = \Sigma_X$), orthogonal ($\Sigma_X \cdot \Sigma_Y = 0$) matrices that describe optical enantiomers. Their racemic mixture at $\vartheta = \pi/4$ is the diagonal matrix of isotropic scattering on a sphere. The off-diagonals are the chiral inductions that arise as cross terms between linear and axial displacements. The imaginary component, $-i\langle md \rangle$, is the matrix element of circular dichroism introduced by Rosenfeld.[40] The real component, $\langle mq \rangle$, which determines linear dichroism, is second order in the scaling factor, $\zeta^2$, hence neglected in the long wave limit applicable to molecular spectroscopy. The signs of these pseudoscalars determine the handedness of the response: $h = (\hat{h}\cdot\hat{n})(\hat{\varepsilon}\cdot\hat{n}) = \text{sign}(\sin\vartheta\cos\vartheta)$ given by the angle $\vartheta$ between dumbbell $\hat{n}$ and the $E$-field. This, and the physical origin of the orientation-dependent signs in eq 3b can be easily seen in the case of linearly polarized light, which as illustrated in Figure 3a, generates R/L-handed helical displacement on a dumbbell oriented along the laboratory $x/y$-axis (for $m, d, q > 0$). Also, although not possible to depict in Euclidian space, in the case of circularly polarized light, $\hat{\varepsilon} = e^{\pm i\vartheta}$ and $\hat{h} = \mp i\hat{\varepsilon}$, the handedness $h = \text{sign}[Im(\mp ie^{\pm i\vartheta})]$ flips upon $\pi/2$ rotation. The more complete representation of the

interaction with arbitrary polarization states of light is obtained in spin space.

The 2D $V$-matrices and their products that are associated with linear and nonlinear light scattering observables find their compact support in the 3D space spanned by the Pauli spin matrices $\sigma_i$, in the special unitary group SU(2):

$$\sigma_0 = \begin{bmatrix} 1 & 0 \\ 0 & 1 \end{bmatrix} \quad \sigma_{z/1} = \begin{bmatrix} 1 & 0 \\ 0 & -1 \end{bmatrix} \quad \sigma_{x/2} = \begin{bmatrix} 0 & 1 \\ 1 & 0 \end{bmatrix}$$

$$\sigma_{y/3} = \begin{bmatrix} 0 & -i \\ i & 0 \end{bmatrix} \tag{4}$$

To the extent that measurements are limited to intensity, polarization states of light can be defined by the Stokes vectors of their field densities, $|\hat{\varepsilon}\rangle\langle\hat{\varepsilon}| = \vec{S}\hat{\sigma}$, and mapped on the Poincaré sphere.[41] Similarly, arbitrary operators can be represented by their spin vectors $\Sigma = \vec{s}\hat{\sigma}$, reducing the observable to the projective measurement $\text{Tr}[(\vec{s}\hat{\sigma})(\vec{S}\hat{\sigma})] = \langle s|S \rangle$. Thus, eq 3a is recast as

$$\Sigma_\vartheta = \frac{1}{2}\sigma_0 + \vec{s}\hat{\sigma}\,\cos(2\vartheta) \tag{5a}$$

where $\sigma_0$ is the identity matrix, and the spin vectors at $\vartheta = 0$ and $\vartheta = \pi/2$ are

$$s_{X/Y} = \pm\left[\frac{(d^2 + q^2 - m^2)}{2N}, \frac{mq}{N}, \frac{-md}{N}\right] \tag{5b}$$

These are the antipodal pure measurement states depicted on the Poincaré sphere in Figure 3b,c. The ODH of circular and linear dichroism along $|\pm 45\rangle$ and $|X/Y\rangle$ polarizations are now simply given by the projections (5b):

$$CD_{X/Y} = CR = \frac{\mp 2md}{N} \tag{6a}$$

$$LD_{X/Y} = LR = \frac{\pm 2mq}{N} \tag{6b}$$

$$LD'_{X/Y} = LR' = \frac{\pm(d^2 + q^2 - m^2)}{N} \tag{6c}$$

Given the idempotency of the $\Sigma_{X/Y}$ matrices (eq 3b), the results hold identically for resonant Raman governed by coherent

absorption−emission, $\langle \Sigma^{\dagger} \Sigma \rangle = \langle \Sigma \rangle$. Thus, CD and LD in eq 6 are identically equated with circular and linear Raman optical activity, CR and LR, respectively. Evidently, a nanodumbbell lying along the laboratory $x$-axis appears L-handed in CR, and when rotated to point along the $y$-axis, it appears R-handed (6a); the converse holds for LR (eqs 6b and 6c).

The spin space representation (eq 5a) reveals that rotation in Euclidian space, from $\vartheta = 0$ to $\vartheta = \pi/2$, effects reflection $\cos(2\vartheta) = 1 \rightarrow -1$ in vector space. The reflection can be enacted on the spin vector $\vec{s}$, which flips from R- to L-hemisphere, or on the Pauli vector $\hat{\sigma}$ (see Figure 3), which inverts the handedness of the frame through the parity transform $\sigma_x, \sigma_y, \sigma_z \rightarrow -\sigma_x, -\sigma_y, -\sigma_z$:

$$\vec{s}_X \xrightarrow{P} \vec{s}_Y = -\vec{s}_X \tag{7}$$

The same interconversion can be accomplished by the quantum time reversal operator, $T = UK$, of body rotation, $U$, followed by complex conjugation $K$:

$$\Sigma_X \xrightarrow{T=UK} \left[ R\left(\frac{\pi}{2}\right) \Sigma_X R\left(-\frac{\pi}{2}\right) \right]^* = [\Sigma_Y^*]^* = \Sigma_Y \tag{8}$$

where $K$ is the reflection $\sigma_y \rightarrow -\sigma_y$ and $U$ is the rotation at the doubled angle around $\sigma_y$. In effect, ODH arises from time-odd $(T_-)$, parity-odd $(P_-)$, and $P_- T_- = PT$-invariant, false chirality.[42] To be in-line with the parity violation energy associated with structural enantiomers, the designation of true chirality is reserved to $T_+, P_-$ systems. The true/false qualifier has significance in ensemble-averaged chiral influence, while by its definition ODH vanishes upon orientational averaging, and since the quadrupole averages out in ensembles, LD is generally ignored in molecular optical activity. As in all tensorial observables, orientational invariants are measured in ensembles. The full tensor is in force when stationary individuals are interrogated. This is recognized in the spectral fluctuations of single molecules: while the spectrum of an ensemble can be used to identify a molecule, the spectrum of the individual depends on the directions of excitation and detection.[43] Similarly, while the ensemble-averaged ROA uniquely identifies structural enantiomers, it should be appreciated that the activity of one molecule is directional. The same holds to a lesser degree on oriented crystals.[44]

## ■ EXPERIMENTAL VERIFICATION

The complete measurement of ODH and its symmetries under the dichotomous time and parity operators is presented in Figure 4, along with the experimental arrangements. The polarization state of the incident light is controlled with a linear polarizer (LP) and quarter-waveplate (QP), and the intensity of backscattered Raman is recorded as a function of rotation angle $\phi$ of the QP. In this arrangement, the Stokes vector $\vec{S}(\phi)$ traces a figure eight on the Poincaré sphere (Figure 4b), and its projection on the spin vectors $I(\phi) = \frac{1}{2} \pm \langle \vec{s} | \vec{S}(\phi) \rangle$ generates the patterns of butterfly and cocoon for a dumbbell aligned along and normal to LP (Figure 4a,c). On the basis of the observed intensities for $|R\rangle$ versus $|L\rangle$ excitation, the butterfly and cocoon are the L- and R-handed enantiomers. Rotation of the LP−QP pair to the laboratory $y$-axis implements the parity transform, as can be inferred by the inversion of the Stokes trajectory (Figure 4b,e). The transform interconverts the cocoon and butterfly, demonstrating odd parity. The data set is reproduced with $m/d = -0.5$, $q/d = -0.5$ as the only fitting
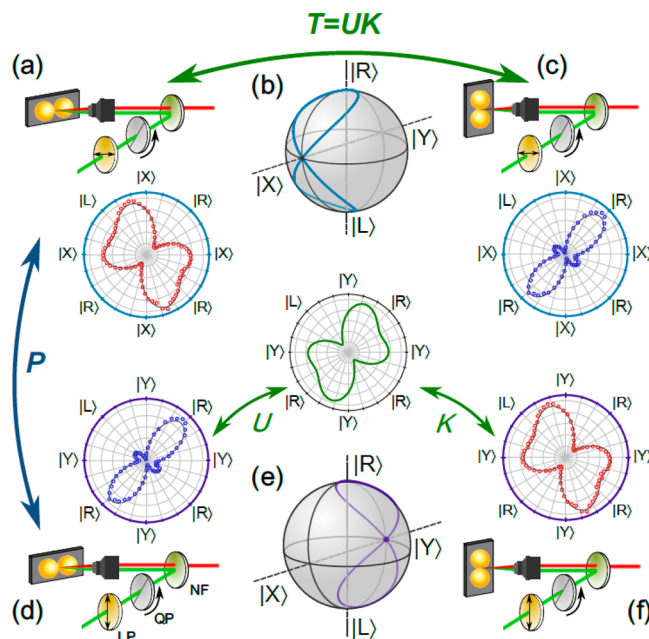


**Figure 4.** ODH and its dichotomous parity and time reversal symmetry. The experiments consist of measuring the total intensity of backscattered Raman scattering through a notch filter (NF), as a function of the polarization of the incident field, which is controlled by the pair of linear polarizer, LP, and quarter-waveplate, QP. The polar plots are the intensities as a function of rotation angle $\phi$ of the QP. Four experimental arrangements are implemented: two orientations of the nantenna, at $\vartheta = 0$ and $\vartheta = \pi/2$, in the left and right column; and two orientations of the LP, at $\vartheta = 0$ and $\vartheta = \pi/2$, in the top and bottom row. Top $\leftrightarrow$ bottom corresponds to the parity transformation, which can be recognized by the inversion of the Stokes trajectories (b and e). The quantum time reversal operation is executed in two steps by the indicated green arrows: $U$ is the $\pi/2$ body rotation followed by complex conjugation $K$, which may be implemented by reversing the sense of the QP rotation. The experimental data (symbols) are reproduced (continuous lines) with $m/d = -0.5$, $q/d = -0.5$ as the two independent variables.

parameters, in perfect agreement for on-resonance excitation and $\zeta = 1$ in eq 1. Using the extracted scattering matrix, we mathematically implement the quantum time reversal $T = UK$ operation in two steps, as in eq 8. As intuition would suggest, $\pi/2$-rotation of the $\Sigma_X$ matrix in Euclidian space does not change handedness. It yields a disoriented (green) butterfly, which upon complex conjugation, $K$, switches handedness. The measurements quantify and explicitly verify the $P_- T_- = PT$-invariance of the interaction.

In Figure 5 we show measurements carried out on five different dumbbells, along with their TEM images. In Figure 5a,b we show the continuous evolution of cocoon to butterfly for oppositely handed dumbbells through complete $\phi$-angle maps recorded at different orientations $\vartheta$ of the dumbbell in the laboratory (see Supporting Information). The two sets are reproduced with $m/d = 0.22$, $q/d = 0.24$ and $m/d = -0.31$, $q/d = -0.71$. The continuous variation in $\vartheta$ corresponds to travel on the chord that connects the antipodal states (Figure 3) and necessarily passes through the achiral origin, $\vec{s} = 0$ at $\vartheta = \pi/4$. In contrast to unitary operations executed by retarders, rotation of the dumbbell in the laboratory frame controls the weights of the mixed state in the projective measurement (eq 3a). The equivalent in physical optics is clearer by setting $m = d = 1$ and
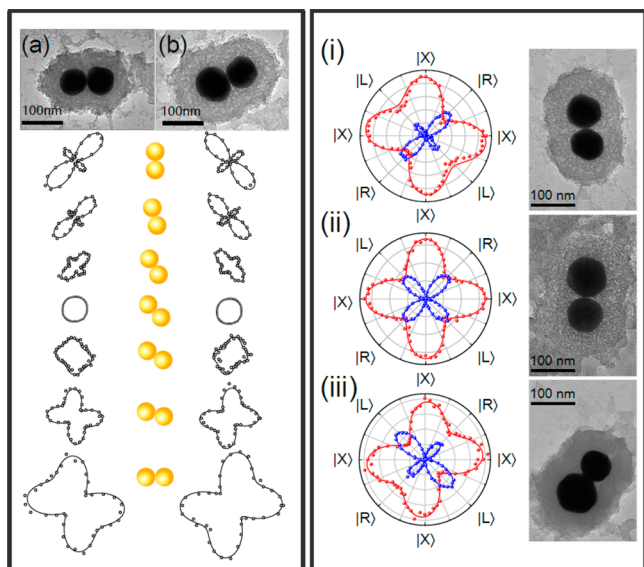
**Figure 5.** Structure, handedness, and chirality. (Left panel) Polar plots of the backscattered Raman intensity as a function of quarter-waveplate angle, $\phi$, are displayed for two oppositely handed nanodumbbells, as a function of their indicated orientations in the laboratory frame. The dimers evolve continuously from L/R-handed to R/L-handed as a function of orientation, passing through the achiral state at $\vartheta = 45°$. (Right panel) Polarization maps of three nanodumbbells when oriented at $\vartheta = 0°$ (red) and $\vartheta = 90°$ (blue). Judging from the R/L-response of the blue maps, (a) is R-handed, $m/d = 0.21$, $q/d = 0.78$; (b) is achiral, $m/d \approx 0$, and (c) is L-handed, $m/d = -0.15$, $q/d = 0.22$.

$q = 0$, upon which the dumbbell appears as the superposition of R- and L-circular polarizers:

$$\Sigma_\vartheta = \cos^2\vartheta |R\rangle\langle R| + \sin^2\vartheta |L\rangle\langle L| \tag{9}$$

and the weighted measurement with the two orthogonal polarizers can be carried out on individual photons. The variation in sign and magnitude of ROA is illustrated by the three examples in the second panel in Figure 5: The first is R-handed ($m/d = 0.21$ and $q/d = 0.78$), the second is practically achiral ($m/d \approx 0$), and the third is L-handed ($m/d = -0.15$, $q/d = 0.22$). Note that the inherent handedness is determined by the relative sign between electric and magnetic displacements. Since the electric susceptibility of gold ($\varepsilon$) is negative at optical frequencies, R-handed nanodumbbells support a negative index $n = \sqrt{\varepsilon\mu}$, and this holds for a broad spectral window: Of the

~50 nanodumbbells investigated, ~40 showed the same handedness at 532 and 633 nm excitation, while ~5 flipped sign between the two wavelengths. Clearly, the typical deviation of nanospheres from sphericity is sufficient to induce chiral response with definite handedness. According to Ruch's classification of the shoe–potato dichotomy,[45] the response is potato-like, where the handedness is not evident by a cursory inspection of shapes.

## CHIRAL CONNECTEDNESS

Since the optical response sustains both CR and LR, it is possible to choose Stokes trajectories that connect the optical enantiomers without passing through an achiral state. Thus, identifying the chiral index of the material polarization by handedness for CR, $h = md/|m\|d|$ and footedness for LR, $f = mq/|m\|q|$, it is sufficient to choose trajectories such that the zero-crossings in $h$ and $f$ do not coincide. Examples are shown in Figure 6, where data recorded along continuous Stokes trajectories are mapped as LR versus CR on the $\hat{\sigma}_x, \hat{\sigma}_y$ plane (Figure 6c). The only trajectories that pass through the achiral origin are those that involve polarization states normal to the $\hat{\sigma}_x, \hat{\sigma}_y$ plane, namely, the $|\pm 45\rangle$ states. Had we also considered the second component of linear dichroism, LR' in eq 6c, the achiral state would be reached only when the Stokes vector is orthogonal to the measurement state, $\langle s|S\rangle = 0$. This cannot be avoided in 2D vector space, e.g., when measurements are limited to linear polarization and the interaction lacks projection along $\sigma_y$. Otherwise, rather than paradoxical, chiral connectedness is the general rule: It is an exceptional trajectory that connects optical enantiomers through the achiral state.

## CHIRAL PLASMONS

Ever since the introduction of the hybridization model,[46] plasmonic resonances of nanodumbbells are identified by analogy to diatomics. Paralleling the construct of a linear combination of atomic orbitals, the $|l_1, m_1 = 0\rangle \pm |l_2, m_2 = 0\rangle$ and $|l_1, m_1 = 1\rangle \mp |l_2, m_2 = 1\rangle$ combinations of nanosphere Mie resonances are assigned to the bonding and antibonding dipolar and quadrupolar plasmons, with interaction energies given by the Coulomb integral of surface charge distributions. A dense manifold of $|l, m_l\rangle$ states cover the spectral range of the four molecular orbitals shown in Figure 7a. Our measurements are entirely limited to the spectral range of the nominally quadrupolar states. They clearly identify chiral and magnetic resonances, which would have been anticipated by considering the leading dipole–dipole tensor that couples plasmons on two
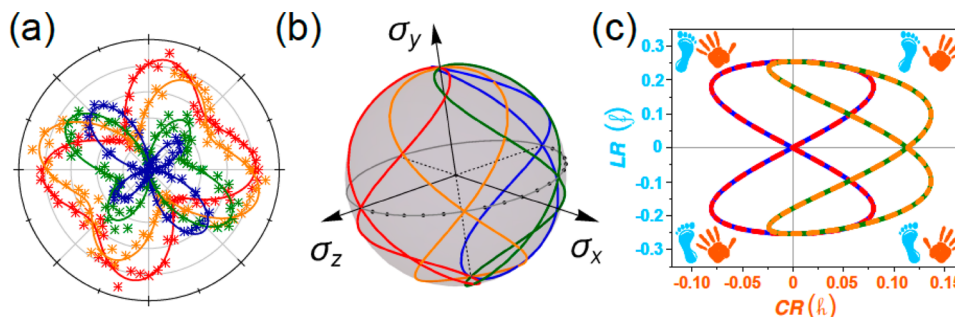


**Figure 6.** Chiral connectedness. (a) Measured backscattered intensities as a function of rotation angle of the QP for four initial orientations of the LP relative to the long axis of the dumbbell: $\varphi = 0°$ (red), 30° (orange), 60° (green), and 90° (blue). (b) Color-coded trajectories of the incident Stokes vector on the Poincaré sphere. (c) Projection of the measurements on the $\sigma_y$, $\sigma_x$ plane, which corresponds to the map of footedness (linear ROA, LR) versus handedness (circular ROA, CR).
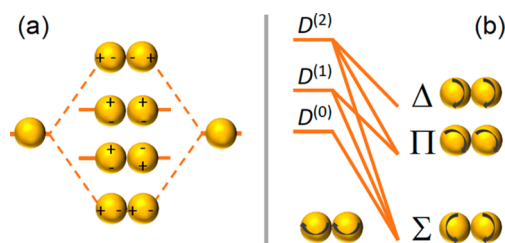
**Figure 7.** Plasmonic resonances. (a) The hybridization model[46] considers the interaction between Cartesian dipoles; (b) the symmetry adapted states of the dipole−dipole interaction in its irreducible spherical representation implies circulating surface current, therefore plasmons that carry angular momentum. The $\Delta$ state is the magnetic plasmon, with cocirculating current $|\pm1, \pm1\rangle$. The $\Pi$ state is helical, with current that involves simultaneous circulation and translation $|\pm1, 0\rangle + |0, \pm1\rangle$ as in Figure 1. The $\Sigma$ state comes in two flavors, the $|0, 0\rangle$ state equivalent to the lowest energy bonding dipolar plasmon in (a) and the counter circulating vortex states $|\pm1, \mp1\rangle$ that approximate magnetic monopoles.

spheres in its irreducible spherical representation.[47] The second rank tensor leads to nine states, $D^{(1)}\otimes D^{(1)} = D^{(2)} + D^{(1)} + D^{(0)}$, which correlate with $\Delta + 2\Pi + 3\Sigma$ states of angular momentum $\Lambda = |m_{l,1} + m_{l,2}| = 2, 1, 0$ along the principle quantization axis (Figure 7b). On nanospheres, these symmetry-adapted states describe surface current: The $\Delta$ state, $|\pm1, \pm1\rangle$, is magnetic, with current cocirculating around the intersphere axis. The $\Pi$ state, $|\pm1, 0\rangle + |0, \pm1\rangle$, is helical, with united sphere limit $Y_{2,\pm1} \approx (x \pm iy)z$. The three $\Sigma$ states with $\Lambda = 0$ come in two flavors: the binding dipolar plasmon, $|0, 0\rangle$, and the vortex states, $|\pm1, \mp1\rangle$, that approximate magnetic monopoles. To the extent that cylindrical symmetry is maintained, $\Lambda \neq 0$ states are doubly degenerate, and the superposition of degenerate $\Lambda_{\pm}$ states leads to the Cartesian multipoles of the hybridization model (Figure 7a). This prevails on achiral nanodumbbells, e.g., Figure 5ii, where the excitation may be assigned to $q_{xz} \propto Y_{2,1} + Y_{2,-1}$ in the united sphere limit. Splitting of $\Lambda_{\pm}$ states is necessary to observe handed response, and the deviation of nanospheres from sphericity is the obvious origin of this broken symmetry. Less clear is the influence of the morphology at the nanometric junction. Nevertheless, the variation in handedness among nanodumbbells confirms the structural origin of the splitting. This hidden asymmetry resolves the contradiction of an achiral structure showing chiral response and at the same time exposes the true challenge that we do not have a quantitative measure of chirality.

## CONCLUDING REMARKS

The phenomena of ODH and chiral connectedness and the distinction between chirality and handedness find satisfactory resolution in the presented ROA measurements on individual nantennas. The contradiction of a nominally achiral structure showing giant optical activity does not have a formal resolution, due to the lack of a quantitative continuous measure of chirality. The challenge may be reduced to the more mundane question of how spherical (achiral) is a nanosphere? The typical gold nanosphere of ∼50 nm radius fails to qualify, as evidenced by the giant chiroptical response of its dimer. Besides the gross size scale $\zeta \approx 1$ essential for retardation to play a role, nanostructuring on much finer scale controls the definite handedness of their interaction with light. This is ultimately traced to the broken degeneracy of $\Lambda \neq 0$ plasmons, which emerges from the treatment of dichrism as the quantum

interference between resonantly prepared electric and magnetic plasmons. although the treatment is formally first order in the spatial dispersion (1), terms up to $\zeta^4$ contribute to the ROA in the limit $\zeta \approx 1$. This generates previously unexplored rich physics and suggests the manipulation of quantum superpositions of plasmons as a powerful paradigm for novel materials applications. A more specific application of chiral plasmons is to amplify the ROA of molecules, which otherwise is a feeble effect in the $\zeta \ll 1$ limit.[48−51] Rather than molecular activity, polarization-based methods are likely to probe the nantenna. Chiral induction should be possible to transfer from the vortex core of plasmons to molecules located at the nanojunction, where a second scaling factor applies: $\zeta_g = 2\pi r/g$, given by molecular dimensions, $r$, and gap length, $g$. This information is encoded in the spectra, as already realized by the observation of magnetic and quadrupolar vibrational Raman spectra at the hot spot of nanojunctions.[43] Clearly, the surface currents depicted in Figure 7 are schematic. There will be a significant concentration of chiral current and vorticity at the junction, with associated large optomagnetic dipoles and monopoles that should be possible to harness. A fully quantum treatment of plasmonics on irregular structures would be invaluable for a rigorous understanding of their dynamics and control over their active optical response.

## METHODS

The measurements are carried out on *trans*-1,2-bis(4-pyridyl)-ethylene-functionalized gold nanosphere dimers that are encapsulated in porous silica. The characteristic sphere diameter is 90 nm, and the typical $SiO_2$ shell thickness is 70 nm. TEM images prior to irradiation show a typical junction gap of ∼1 nm. Commonly, postirradiation images show necking and partial fusion of the junction, caused in part by electron bombardment during the recording of TEM images. This consideration predicates the measurement protocol, which consists of (a) SEM mapping (∼5 nm resolution) of the drop-cast sample on a silicon nitride grid, (b) remapping on the optical microscope using backscattered light, (c) optical measurements on colocated individual particles with alignment in the laboratory frame known to within $\pm5°$, and (d) TEM characterization of the studied nanostructures. The Raman spectra are carried out in the backscattering geometry, with the sample mounted on an inverted optical microscope (Olympus IX71, NA = 0.65 objective). CW diode lasers operating either at 532 or 633 nm are used as excitation source. The backscattered Raman signal is separated from the Rayleigh light using two notch filters (Semrock, 1:106 extinction ratio), then dispersed in a 0.5 m monochromator, and recorded on a CCD array (Andor V401-BV).

## ASSOCIATED CONTENT

**Ⓢ Supporting Information**

The Supporting Information is available free of charge on the ACS Publications website at DOI: 10.1021/acsphotonics.6b00733.

Raw Raman spectra, recorded as a function of rotation angle of quarter-waveplate $\phi$ and orientation angle $\vartheta$ of the dumbbell in the laboratory; stepwise delineation of the procedures used in the data reduction and construction of the polar plots presented in the main body of the paper; specifically, the data set for nanodumbbells shown in Figure 5i−iii; $\phi$, $\vartheta$ maps of

all molecular vibrations and the electronic Raman spectrum of the background (PDF)

# ■ AUTHOR INFORMATION

**Corresponding Author**

*E-mail (V. A. Apkarian): aapkaria@uci.edu.

**ORCID**

V. Ara Apkarian: 0000-0002-7648-5230

**Author Contributions**

M.B., K.R., and E.H. carried out the experimental measurements and analysis. K.R. conceived of the orientation dependence measurements. V.A.A. planned and guided the research and coauthored the manuscript with M.B. and K.R.

**Notes**

The authors declare no competing financial interest.

# ■ REFERENCES

(1) Landau, L. D.; Lifshitz, E. M. *Electrodynamics of Continuous Media*; Butterworth-Heinemann: Oxford, 1984; Chapter 9.

(2) Novotny, L.; van Hulst, N. F. Antennas for Light. *Nat. Photonics* **2011**, *5*, 83−90.

(3) Liu, Y.; Zhang, X. Metamaterials: A New Frontier of Science and Technology. *Chem. Soc. Rev.* **2011**, *40*, 2494−2507.

(4) Merlin, R. Metamaterials and the Landau-Lifshitz Permeability Argument: Large Permittivity Begets High-Frequency Magnetism. *Proc. Natl. Acad. Sci. U. S. A.* **2009**, *106*, 1693−1698.

(5) Agranovich, V. M.; Gartstein, Y. N. Electrodynamics of Metamaterials and the Landau-Lifshitz Approach to the Magnetic Permeability. *Metamaterials* **2009**, *3*, 1−9.

(6) Engheta, N.; Ziolkowski, R. W. *Metamaterials: Physics and Engineering Explorations*; John Willey & Sons, Inc., 2006.

(7) Boriskina, S. V; Zheludev, N. I. *Singular and Chiral Nanoplasmonics*; Pan Stanford, Singapore: Singapore, 2014.

(8) Veselago, V. G. The Electrodynamics of Substances with Simultaneously Negative Values of E and U. *Sov. Phys. Usp.* **1968**, *10*, 509−514.

(9) Pendry, J. B.; Holden, A. J.; Robbins, D. J.; Stewart, W. J. Magnetism from Conductors and Enhanced Non-Linear Phenomena. *IEEE Trans. Microwave Theory Tech.* **1999**, *47*, 2075−2084.

(10) Smith, D. R.; Smith, D. R.; Padilla, W. J.; Padilla, W. J.; Vier, D. C.; Vier, D. C.; Nemat-Nasser, S. C.; Nemat-Nasser, S. C.; Schultz, S.; Schultz, S. Composite Medium with Simultaneously Negative Permeability and Permittivity. *Phys. Rev. Lett.* **2000**, *84*, 4184−4187.

(11) Schurig, D.; Mock, J. J.; Justice, B. J.; Cummer, S. a; Pendry, J. B.; Starr, a F.; Smith, D. R. Metamaterial Electromagnetic Cloak at Microwave Frequencies. *Science* **2006**, *314*, 977−980.

(12) Fedotov, V. A.; Mladyonov, P. L.; Prosvirnin, S. L.; Rogacheva, A. V.; Chen, Y.; Zheludev, N. I. Asymmetric Propagation of Electromagnetic Waves through a Planar Chiral Structure. *Phys. Rev. Lett.* **2006**, *97*, 167401.

(13) Sounas, D. L.; Caloz, C.; Alù, A. Giant Non-Reciprocity at the Subwavelength Scale Using Angular Momentum-Biased Metamaterials. *Nat. Commun.* **2013**, *4*, 2407.

(14) Menzel, C.; Helgert, C.; Rockstuhl, C.; Kley, E. B.; Tünnermann, A.; Pertsch, T.; Lederer, F. Asymmetric Transmission of Linearly Polarized Light at Optical Metamaterials. *Phys. Rev. Lett.* **2010**, *104*, 253902.

(15) Plum, E.; Liu, X. X.; Fedotov, V. A.; Chen, Y.; Tsai, D. P.; Zheludev, N. I. Metamaterials: Optical Activity without Chirality. *Phys. Rev. Lett.* **2009**, *102*, 113902.

(16) Pendry, J. B. A Chiral Route to Negative Refraction. *Science* **2004**, *306*, 1353−1355.

(17) Valev, V. K.; Baumberg, J. J.; Sibilia, C.; Verbiest, T. Chirality and Chiroptical Effects in Plasmonic Nanostructures: Fundamentals, Recent Progress, and Outlook. *Adv. Mater.* **2013**, *25*, 2517−2534.

(18) Lu, X.; Wu, J.; Zhu, Q.; Zhao, J.; Wang, Q.; Zhan, L.; Ni, W. Circular Dichroism from Single Plasmonic Nanostructures with Extrinsic Chirality. *Nanoscale* **2014**, *6*, 14244−14253.

(19) Ferry, V. E.; Smith, J. M.; Alivisatos, A. P. Symmetry Breaking in Tetrahedral Chiral Plasmonic Nanoparticle Assemblies. *ACS Photonics* **2014**, *1*, 1189−1196.

(20) Drezet, A.; Genet, C.; Laluet, J.-Y.; Ebbesen, T. W. Optical Chirality without Optical Activity: How Surface Plasmons Give a Twist to Light. *Opt. Express* **2008**, *16*, 12559−12570.

(21) Chuntonov, L.; Haran, G. Maximal Raman Optical Activity in Hybrid Single Molecule-Plasmonic Nanostructures with Multiple Dipolar Resonances. *Nano Lett.* **2013**, *13*, 1285−1290.

(22) Papakostas, A.; Potts, A.; Bagnall, D. M.; Prosvirnin, S. L.; Coles, H. J.; Zheludev, N. I. Optical Manifestations of Planar Chirality. *Phys. Rev. Lett.* **2003**, *90*, 107404.

(23) Kuwata-Gonokami, M.; Saito, N.; Ino, Y.; Kauranen, M.; Jefimovs, K.; Vallius, T.; Turunen, J.; Svirko, Y. Giant Optical Activity in Quasi-Two-Dimensional Planar Nanostructures. *Phys. Rev. Lett.* **2005**, *95*, 227401.

(24) Rogacheva, A. V.; Fedotov, V. A.; Schwanecke, A. S.; Zheludev, N. I. Giant Gyrotropy due to Electromagnetic-Field Coupling in a Bilayered Chiral Structure. *Phys. Rev. Lett.* **2006**, *97*, 177401.

(25) Schäferling, M.; Yin, X.; Giessen, H. Formation of Chiral Fields in a Symmetric Environment. *Opt. Express* **2012**, *20*, 26326−26336.

(26) Yampolsky, S.; Fishman, D. A.; Dey, S.; Hulkko, E.; Banik, M.; Potma, E. O.; Apkarian, V. A. Seeing a Single Molecule Vibrate through Time-Resolved Coherent Anti-Stokes Raman Scattering. *Nat. Photonics* **2014**, *8*, 650−656.

(27) Alù, A.; Engheta, N. Hertzian Plasmonic Nanodimer as an Efficient Optical Nanoantenna. *Phys. Rev. B: Condens. Matter Mater. Phys.* **2008**, *78*, 195111.

(28) Gersten, J. I.; Nitzan, A. Photophysics and Photochemistry near Surfaces and Small Particles. *Surf. Sci.* **1985**, *158*, 165−189.

(29) Barron, L. D. Raman Optical Activity: A New Probe of Stereochemistry and Magnetic Structure. *Acc. Chem. Res.* **1980**, *13*, 90−96.

(30) Yang, W.; Hulteen, J.; Schatz, G. C.; Van Duyne, R. P. A Surface-Enhanced Hyper-Raman and Surface-Enhanced Raman Scattering Study of Trans-1, 2-Bis (4-Pyridyl) Ethylene Adsorbed onto Silver Film over Nanosphere Electrodes. Vibrational Assignments: Experiment and Theory. *J. Chem. Phys.* **1996**, *104*, 4313−4323.

(31) Dey, S.; Banik, M.; Hulkko, E.; Rodriguez, K.; Apkarian, V. A.; Galperin, M.; Nitzan, A. Observation and Analysis of Fano-like Lineshapes in the Raman Spectra of Molecules Adsorbed at Metal Interfaces. *Phys. Rev. B: Condens. Matter Mater. Phys.* **2016**, *93*, 35411.

(32) Crampton, K. T.; Zeytunyan, A.; Fast, A. S.; Ladani, F. T.; Alfonso-Garcia, A.; Banik, M.; Yampolsky, S.; Fishman, D. A.; Potma, E. O.; Apkarian, V. A. Ultrafast Coherent Raman Scattering at Plasmonic Nanojunctions. *J. Phys. Chem. C* **2016**, *120*, 20943−20953.

(33) Mason, S. F. *Molecular Optical Activity and the Chiral Discriminations*; Cambridge University Press: Cambridge, 2009.

(34) Wagniere, G. H. *On Chirality and the Universal Asymmetry: Reflections on Image and Mirror Image*; Wiley-VCH: Zurich, 2007.

(35) Lord Kelvin. *Baltimore Lectures*; C. J. Clay and Sons: London, 1904.

(36) Efrati, E.; Irvine, W. Orientation-Dependent Handedness and Chiral Design. *Phys. Rev. X* **2014**, *4*, 11003.

(37) Fowler, P. W. Quantification of Chirality: Attempting the Impossible. *Symmetry Cult. Sci.* **2005**, *16*, 321−334.

(38) Millar, G.; Weinberg, N.; Mislow, K. On the Osipov–Pickup–Dunmur Chirality Index: Why Pseudoscalar Functions Are Generally Unsuitable to Quantify Chirality. *Mol. Phys.* **2005**, *103*, 2769–2772.

(39) Schatz, G. C.; Ratner, M. A. *Quantum Mechanics in Chemistry*; Dover Publications, 2002.

(40) Rosenfeld, L. Quantenmechanische Theorie Der Naturlichen Optischen Aktivitaet von Fluessigkeiten Und Gasen. *Eur. Phys. J. A* **1929**, *52*, 161–174.

(41) Steane, A. M. An Introduction to Spinors. *arXiv:1312.3824v1* 2013, 1–23.

(42) Barron, L. D. True and False Chirality and Absolute Asymmetric Synthesis. *J. Am. Chem. Soc.* **1986**, *108*, 5539–5542.

(43) Banik, M.; El-Khoury, P. Z.; Nag, A.; Rodriguez-Perez, A.; Guarrottxena, N.; Bazan, G. C.; Apkarian, V. A. Surface-Enhanced Raman Trajectories on a Nano-Dumbbell: Transition from Field to Charge Transfer Plasmons as the Spheres Fuse. *ACS Nano* **2012**, *6*, 10343–10354.

(44) Buckingham, A. D.; Dunn, M. B. Optical Activity of Oriented Molecules. *J. Chem. Soc. A* **1971**, 1988–1991.

(45) King, R. B. Chirality and Handedness–The Ruch "shoe-Potato" Dichotomy in the Right-Left Classification Problem. *Ann. N. Y. Acad. Sci.* **2003**, *988*, 158–170.

(46) Nordlander, P.; Oubre, C.; Prodan, E.; Li, K.; Stockman, M. I. Plasmon Hybridization in Nanoparticle Dimers. *Nano Lett.* **2004**, *4*, 899–903.

(47) Jackson, J. D. *Classical Electrodynamics*; 3rd ed.; John Wiley & Sons, Inc., 1999.

(48) Efrima, S. The Effect of Large Electric Field Gradients on the Raman Optical Activity of Molecules Adsorbed on Metal Surfaces. *Chem. Phys. Lett.* **1983**, *102*, 79–82.

(49) Jensen, L. Surface-Enhanced Vibrational Raman Optical Activity: A Time-Dependent Density Functional Theory Approach. *J. Phys. Chem. A* **2009**, *113*, 4437–4444.

(50) Acevedo, R.; Lombardini, R.; Halas, N. J.; Johnson, B. R. Plasmonic Enhancement of Raman Optical Activity in Molecules near Metal Nanoshells. *J. Phys. Chem. A* **2009**, *113*, 13173–13183.

(51) Govorov, A. O.; Fan, Z.; Hernandez, P.; Slocik, J. M.; Naik, R. R. Theory of Circular Dichroism of Nanomaterials Comprising Chiral Molecules and Nanocrystals: Plasmon Enhancement, Dipole Interactions, and Dielectric Effects. *Nano Lett.* **2010**, *10*, 1374–1382.